



Publication Year	2019
Acceptance in OA	2020-12-21T10:20:17Z
Title	Mineralogical mapping of Coniraya quadrangle of the dwarf planet Ceres
Authors	RAPONI, Andrea, CARROZZO, FILIPPO GIACOMO, ZAMBON, Francesca, DE SANCTIS, MARIA CRISTINA, CIARNIELLO, Mauro, FRIGERI, ALESSANDRO, Ammannito, E., TOSI, Federico, Combe, J. -Ph., Longobardo, A., PALOMBA, Ernesto, Pieters, C. M., Raymond, C. A., Russell, C. T.
Publisher's version (DOI)	10.1016/j.icarus.2017.10.023
Handle	http://hdl.handle.net/20.500.12386/29037
Journal	ICARUS
Volume	318

Mineralogical mapping of Coniraya Quadrangle of the Dwarf Planet Ceres

A. Raponi^a, F.G. Carrozzo^a, F. Zambon^a, M.C. De Sanctis^a, M. Ciarniello^a, A. Frigeri^a, E. Ammannito^b,
F. Tosi^a, J.-Ph. Combe^c, A. Longobardo^a, E. Palomba^a, C.M. Pieters^d, C.A. Raymond^e, C.T. Russell^f.

^a INAF-IAPS Istituto di Astrofisica e Planetologia Spaziali, Via del Fosso del Cavaliere, 100, I-00133 Rome, Italy;

^b Italian Space Agency (ASI), Via del Politecnico snc, I-00133 Rome, Italy;

^c Bear Fight Institute, 22, Fiddler's Road, P.O. Box 667, Winthrop, WA, 98862, USA;

^d Department of Earth, Environmental and Planetary Sciences, Brown University, 324 Brook Street, Providence, RI 02912, USA;

^e NASA/Jet Propulsion Laboratory and California Institute of Technology, 4800 Oak Grove Drive, Pasadena, CA 91109, USA;

^f Institute of Geophysics and Planetary Physics, University of California at Los Angeles, 3845 Slichter Hall, 603 Charles E. Young Drive, East, Los Angeles, CA 90095-1567, USA.

Proposed Running Head: Mineralogical analysis of the Ac-H-2 Coniraya quadrangle.

*** Corresponding author:** Dr. Andrea Raponi

INAF-IAPS Istituto di Astrofisica e Planetologia Spaziali

Via del Fosso del Cavaliere, 100, I-00133 Rome, Italy

Email : andrea.raponi@iaps.inaf.it

Abstract

Ceres has been explored by NASA/Dawn spacecraft, which allowed for the discovery of the main mineralogical and compositional characteristics of Ceres' surface. Here, we use mainly data from the Visible and InfraRed imaging spectrometer (VIR) in order to investigate the main spectral characteristics of the quadrangle Ac-H-2 Coniraya, one of the 15 quads in which Ceres' surface has been divided. Coniraya quadrangle is characterized by the presence of mostly highly degraded impact craters of diameters between 50 and 200 km and clusters of small to midsize impact craters. Although the composition over the quadrangle appears to be quite uniform, significant differences have been detected between different craters by spectral parameters analysis and spectral modeling. Ernutet crater presents two regions with very peculiar band at 3.4 μm , typical of organics aliphatic material. One region result to be correlated with larger amount of carbonates, the other region does not present such correlation. Ikapati crater shows strong absorption bands at 4.0 μm , indicating the presence of Na-carbonates in the floor and ejecta. Ikapati, Gaue and other craters present smaller spectral features of NH_4 and/or OH stretching, suggesting a volatile depletion process induced by the heating of the impact event.

39
40
41
42
43
44
45
46
47
48
49
50
51
52
53
54
55
56
57
58
59
60
61
62
63
64
65
66
67
68
69
70
71
72
73
74
75
76
77
78
79
80
81
82
83
84

1. Introduction

NASA's Dawn spacecraft arrived at dwarf planet 1-Ceres on March 6, 2015, with its scientific payload: the Visible and near-InfraRed imaging spectrometer (VIR) (De Sanctis et al., 2011), the Gamma Ray and Neutron Detector (GRaND) (Prettyman et al., 2011), and the Framing Camera (FC) (Sierks et al., 2011), along with the radio science package (Konopliv et al., 2011).

Here, we use data returned by VIR and FC instruments in order to study the mineralogical composition of the quadrangle Ac-H-2 'Coniraya' (21-66 °N and 0-90 °E), which is one of four quadrangles in Ceres' northern hemisphere.

Ceres' surface shows ubiquitous absorption bands at 2.7 μm (OH stretching in Mg-phyllosilicates) and 3.1 μm related NH₄-phyllosilicates, respectively (De Sanctis et al., 2015; Ammannito et al., 2016).

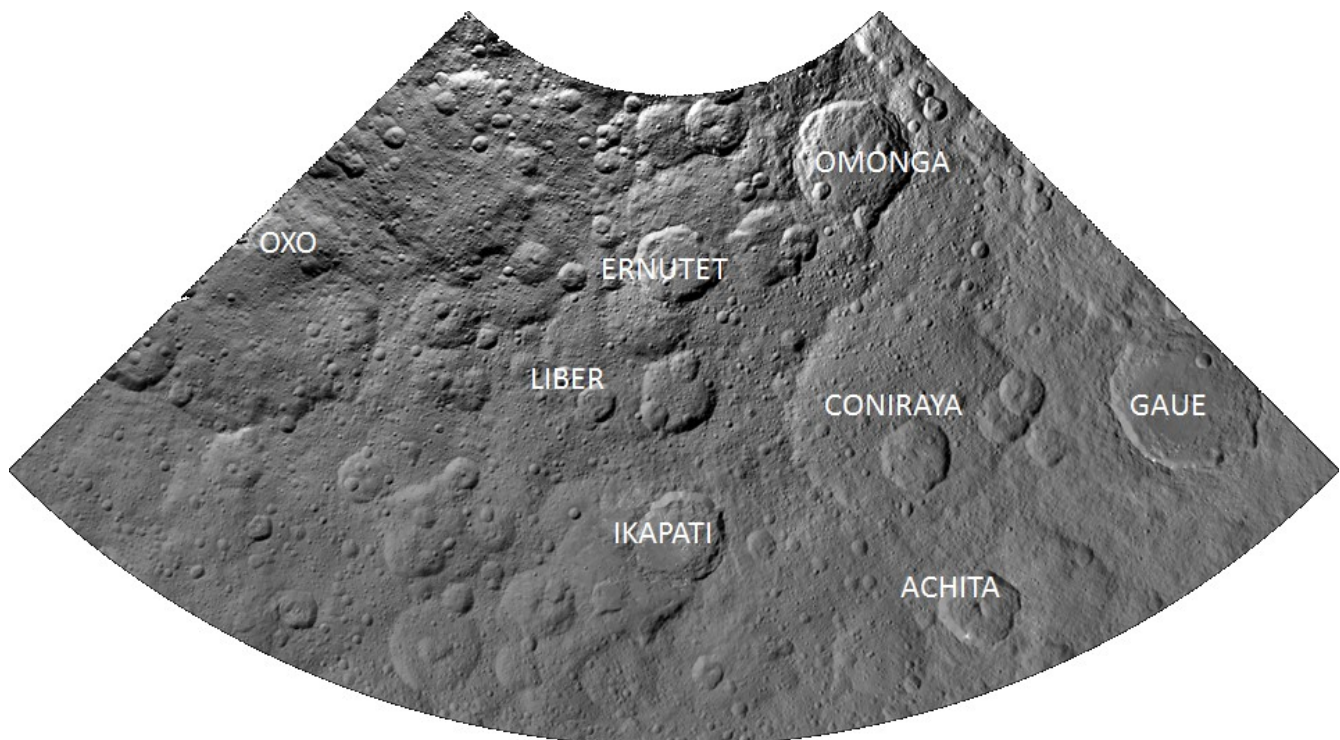
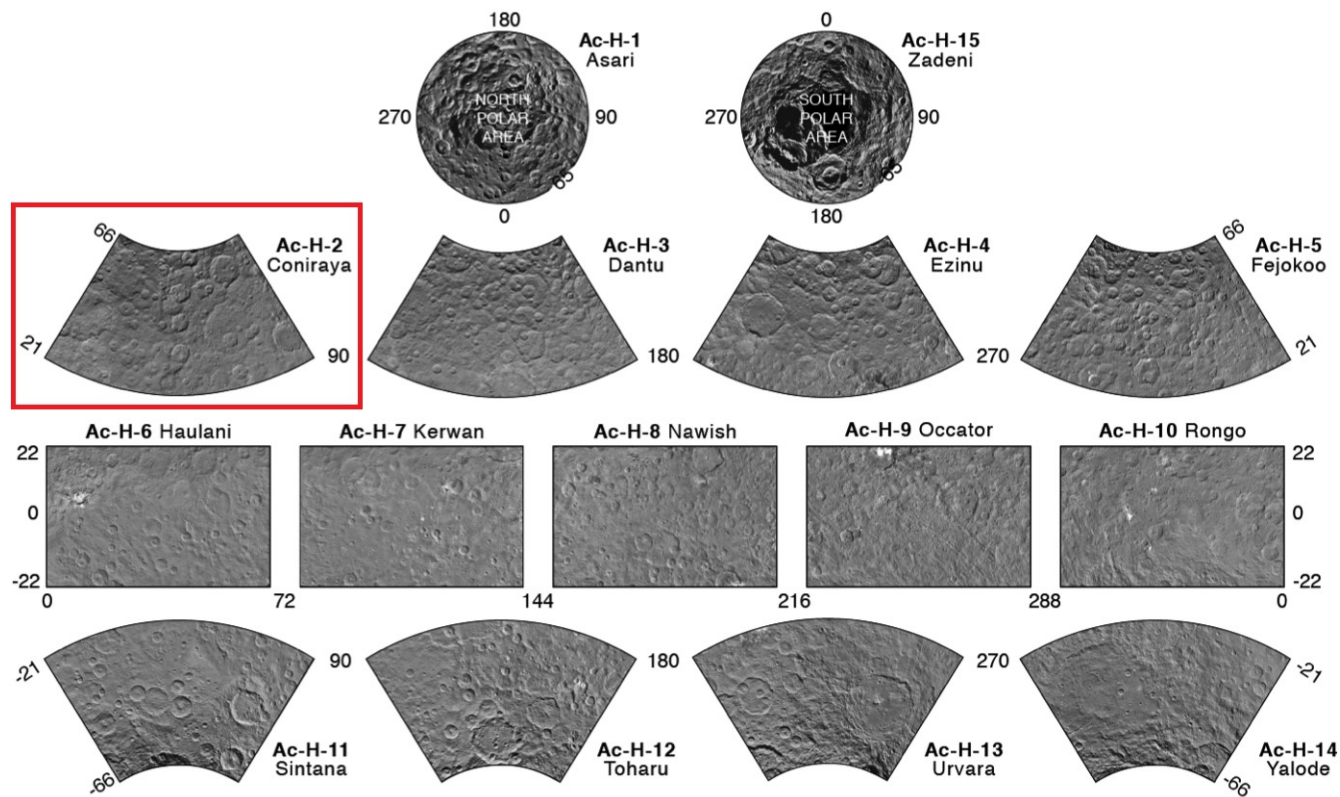
The thermally-corrected reflectance spectrum of Ceres shows several distinct absorption bands at 3.3-3.5, and 3.95 μm , related to the presence of Mg-carbonates and NH₄-phyllosilicates (De Sanctis et al., 2015).

Although spectral properties of Ceres' surface are quite uniform, there are some peculiar areas where significant differences have been detected in spectral parameters such as slopes, albedo, band depths and band centers. The case that stands out above the surrounding terrains are the bright areas ("Ceralia and Vinalia faculae") in the Occator crater (De Sanctis et al., 2016; Raponi et al., 2017; Longobardo et al., this issue), where the albedo is 5-10 times higher than the average surface. The OH feature in these faculae is shifted from 2.72 to 2.76 μm , indicating the presence of Al-phyllosilicates, while the carbonate features are shifted from 3.95 to 4.0 μm with increasing band depth, suggesting a large abundance of Na-carbonates (De Sanctis et al., 2016). Additionally to the Occator crater, other areas show a signature of Na-carbonates (Carrozzo et al., 2017), e.g., Ikapati crater, located in the 'Coniraya' quadrangle, which is part of the analysis done in the present work.

Knowledge of the mineralogy of Ceres has been enriched by the discovery of organic material mainly in the form of aliphatic material (De Sanctis et al., 2017) near the Ernutet crater (latitude $\sim 53^\circ\text{N}$, longitude 45.5°E , diameter 53.4 km), contained in Coniraya quadrangle .

Oxo crater is another interesting region, which the Coniraya quadrangle shares with the Ac-H-5 'Fejokoo' crater, but which is mostly located in the latter. It is a fresh crater where a large amount of water ice has been detected (Combe et al., 2016; Raponi et al., 2016; Combe et al., this issue). Moreover, it is the second brightest feature on Ceres after the bright material of the Occator crater. Water ice was detected near the southern rim and corresponds to the high albedo materials on the floor of the crater (Combe et al., 2016). The water ice location is entirely in the 'Fejokoo' quadrangle. We refer to Combe et al. (this issue), and Singh et al. (this issue) for further details about this crater.

In section 2, we present the dataset and the methodology used to perform the spectral analysis. In section 3, the thermal emission removal, relevant for the discussion of the spectra in the thermal emission range, is described. In section 4, we give a general view of the quadrangle, discussing the spectral parameters, such as band centers, band depth, spectral slope and albedo. In section 5 we present a quantitative analysis of abundances of the main minerals identified as component of surface materials, by means of the Hapke radiative transfer model. The main findings are discussed in section 6, under the general context of Ceres' surface.



87 **Figure 1.** Upper panel: figure adapted from Roatsch et al. (2016), showing the 15-quadrangle scheme in which
 88 Ceres' surface has been divided. The Coniraya quadrangle, highlighted in red, is the main focus of this study and
 89 is located at 0° - 90°, 21° - 66° N. Bottom: Dawn Framing Camera clear filter LAMO base map mosaic in the
 90 Lambert Conical projection, with 35 m/pixel resolution. The names of the main craters are indicated.
 91
 92

85
86

87
88
89
90
91
92

2. Data analysis description

The present work uses the dataset acquired by VIR, the mapping spectrometer of the Dawn mission (Russell and Raymond, 2011; De Sanctis et al., 2011). Images provided by the Dawn Framing Camera (Sierks et al., 2011) are also used for context and morphological analysis.

VIR is an imaging spectrometer operating in two channels: the visible channel, ranging between 0.25-1.05 μm , and the infrared channel, between 1.0-5.1 μm . VIR is capable of high spatial (IFOV= 250 $\mu\text{rad}/\text{pixel}$, FOV= 64×64 mrad) and spectral ($\Delta\lambda_{\text{VIS}} = 1.8$ nm/band; $\Delta\lambda_{\text{IR}} = 9.8$ nm/band) performances, allowing for the identification of spectral features in order to derive the composition, structure of the surface, and thermal emission.

VIR acquired data of Ceres during all of the mission phases: Survey (spacecraft altitude 4350 km), High Altitude Mapping Orbit (HAMO) (spacecraft altitude 1450 km) and Low Altitude Mapping Orbit (LAMO) (spacecraft altitude 370 km) (Russell and Raymond, 2011). Here, we used the HAMO dataset with nominal spatial resolution of 360-400 m/pix.

The calibrated data (Filacchione et al., 2011, Ammannito et al., 2011) are cleaned for artifacts with the procedure described in Carrozzo et al. (2016). In order to analyze the spectral signature in the range of wavelengths affected by thermal emission (usually from 3.2 μm longward), we use the method described in section 3 to remove the thermal emission. In this paper photometric effects are corrected for both topographic variations and physical characteristics of the regolith using the Hapke approach (Ciarniello et al., 2016). However, other methods for photometric correction can be applied (Longobardo et al., in preparation), yielding similar results, but they are not considered in this work.

To analyze a large dataset like the one considered in this work, we developed an automatic data process able to return different spectral indicators from Ceres observations. This algorithm allows us to map the spatial distribution of each spectral indicator across the surface (for more details about this algorithm, see Frigeri et al., this issue). The main spectral parameters selected are:

- photometrically corrected reflectance at 1.2 μm ,
- spectral slope in the range 1.891-1.163 μm ,
- band depths of phyllosilicate bands at 2.7,
- band depths of NH_4 -phyllosilicate bands at 3.1 μm ,
- band depths at 3.4 μm ,

In the present work we also consider the band depths of carbonates at 3.3-3.5 μm , and 3.9 μm (not computed in the automatic algorithm).

3. Thermal removal

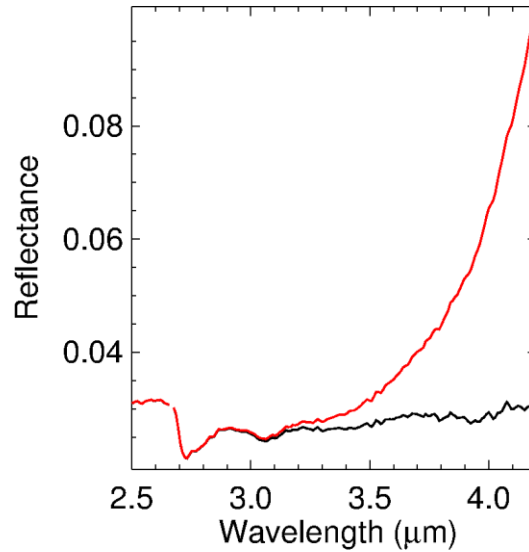
The observed spectra of Ceres' surface are affected by thermal emission from ~ 3.2 μm longward. The radiance of the thermal emission hides the absorption bands and prevents a comparison with laboratory data. We implemented a proper algorithm in order to remove the thermal emission while preserving the spectral features present in the spectra. This is made by modeling the total radiance as the sum of the solar radiance reflected by the surface and the thermal emission of the surface itself, and then performing the removal of the latter, as follows:

- The model of the solar reflected radiance is produced by a model of reflectance of the surface, multiplied by the solar irradiance at Ceres' heliocentric distance. To be consistent with the spectral modeling discussed in Section 5 we used the same reflectance model to estimate the reflectance level in the thermal emission range.
- The Planck function is summed up to this model in order to fit the total radiance level. Free parameters of the Planck function are temperature and emissivity. Their retrieved values are not discussed in the present work.

140
141
142
143
144
145
146
147

- Once the Planck function has been derived, we subtract it from the total measured radiance, and we divide the result by the solar irradiance to obtain the reflectance in the whole range.

The reflectance continuum in the thermal emission range, after removal of the Planck function, could be over or underestimated depending on the reflectance model used. However, the measured spectral features are not affected by this uncertainty. Typical result of thermal removal is shown in Fig. 2. The spectral range 3.3 – 4.2 μm , after thermal removal, present the absorption bands of the carbonates at 3.5 μm and 3.95 μm (see also Fig. 8).

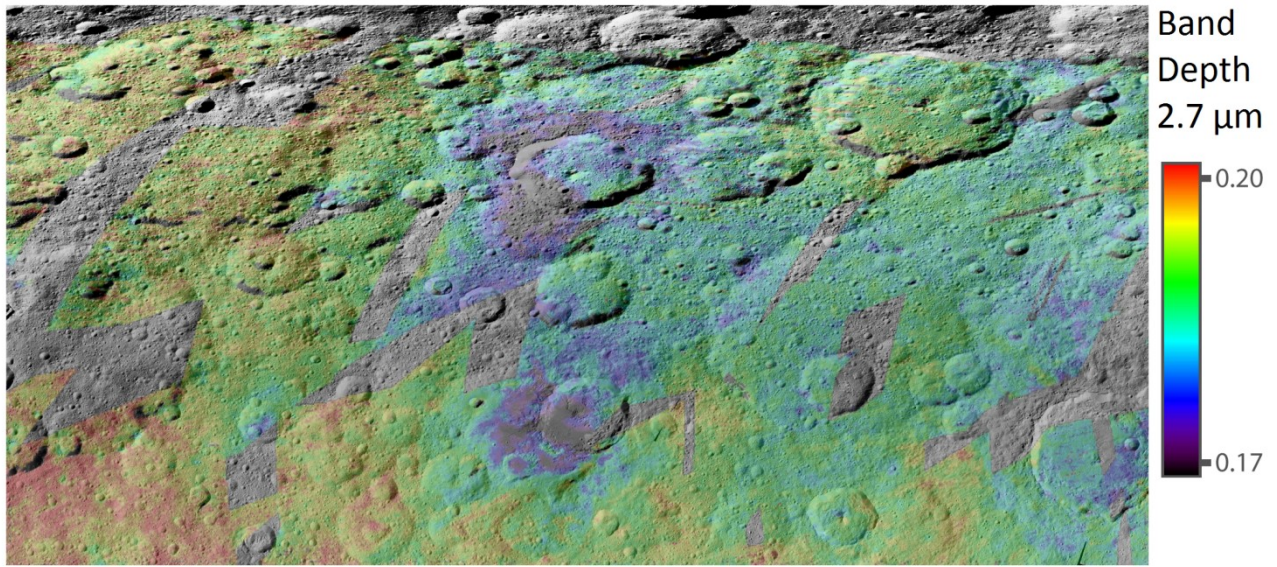


148
149
150
151
152
153
154
155
156
157
158
159
160
161
162
163
164
165
166
167

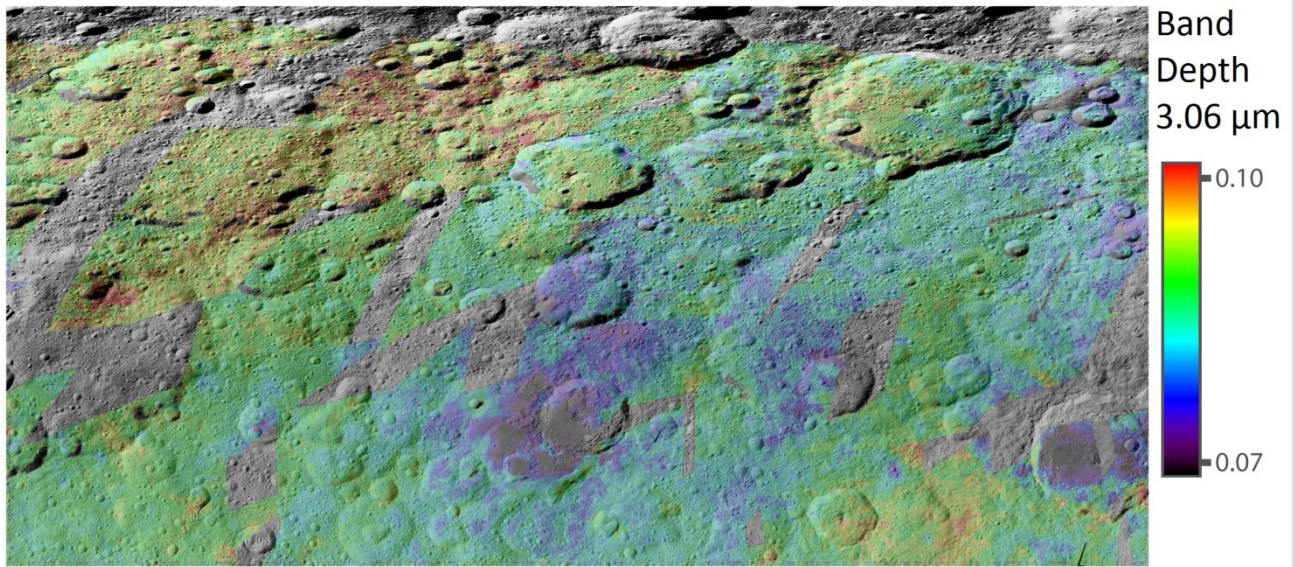
Figure 2. Thermal emission removal of a typical spectrum of the average surface of Ceres. Red and black lines are respectively the reflectance spectra before and after thermal emission removal.

4. Spectral analysis

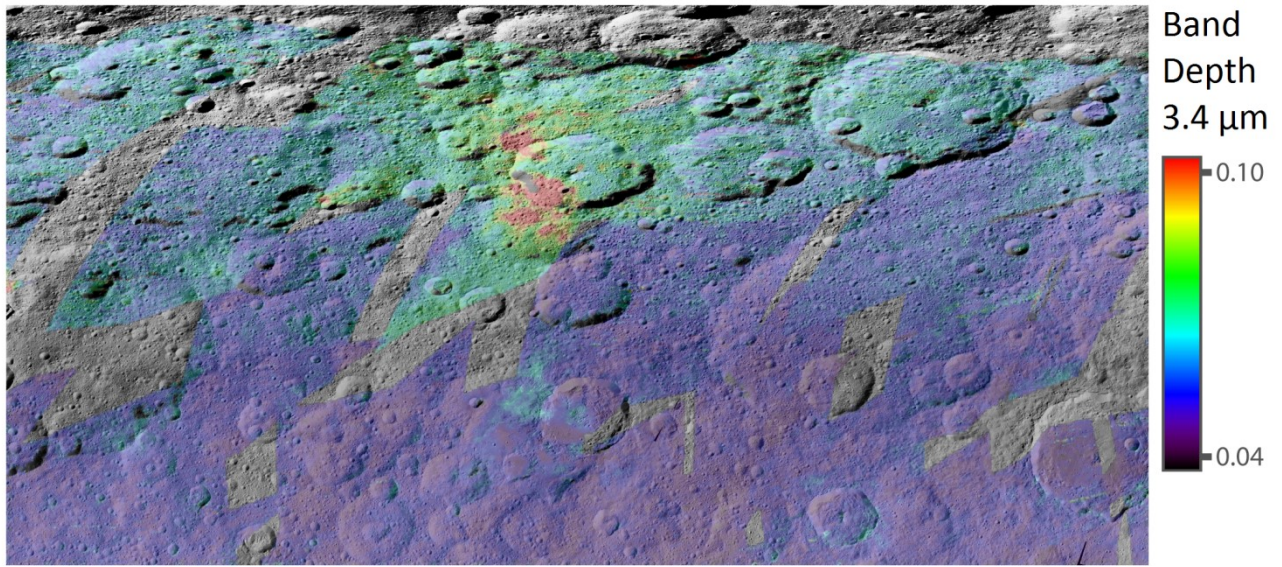
The quadrangle is dominated by mostly highly degraded impact craters of diameters between 50 and 200 km and clusters of small to midsize impact craters. The seven most prominent impact craters have been named Coniraya, Gaue, Omonga, Ikapati, Achita, Ernutet, and Liber (see Fig. 1). Coniraya is the largest impact crater in the quadrangle, while Gaue and Ikapati craters are the freshest large impact craters. We refer to Pasckert et al. (2016) for a complete geological mapping of the Coniraya quadrangle.



168
169 **Figure 3.** The band depth at 2.7 μm shows the abundance of Mg-phyllsilicates.
170

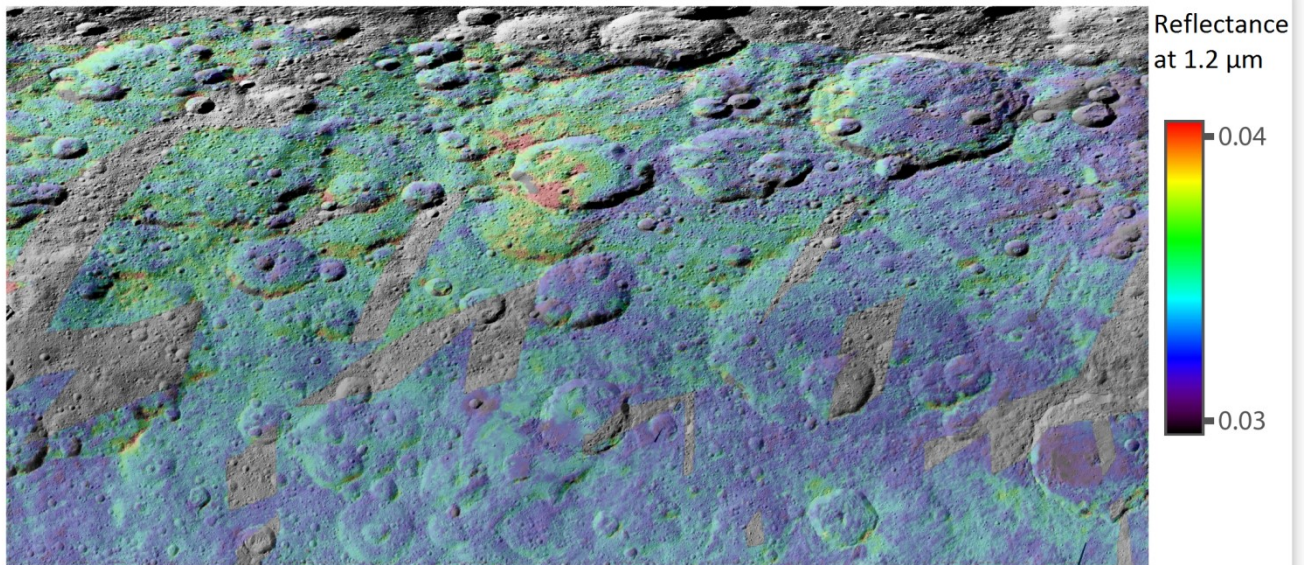


171
172 **Figure 4.** The band depth at 3.1 μm is indicative of the NH4-phyllsilicates abundance.
173
174



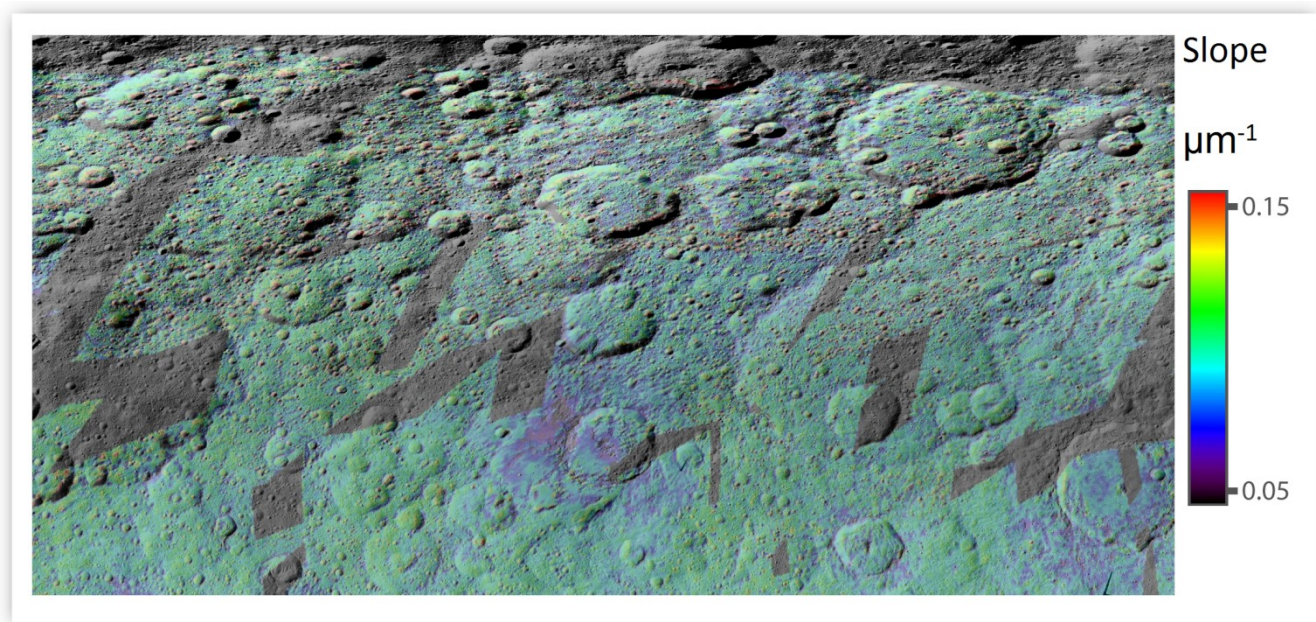
175
176
177

Figure 5. The band depth at 3.4 μm is linked with the abundance of organic materials.



178
179
180

Figure 6. Coniraya photometrically corrected reflectance map at 1.2 μm .



181
 182 **Figure 7.** Coniraya 1.891-1.163 μm spectral slope map. To calculate the spectral slope, we use the definition
 183 used by Cuzzi et al. (2009), and Filacchione et al. (2012): $\text{Slope} = (R_{\lambda_2} - R_{\lambda_1}) / (\lambda_2 - \lambda_1) / R_{\lambda_1}$, where $\lambda_1 = 1.163$
 184 μm , $\lambda_2 = 1.891 \mu\text{m}$, and R_{λ} is the reflectance at λ .

185
 186
 187 Maps showing band parameters (Figs.3-7) have been computed from VIR data acquired during the
 188 survey and HAMO phase.

189
 190 We consider thermally corrected spectra as discussed in section 3. Before producing the maps, the
 191 Hapke photometric correction has been applied to the VIR data (Hapke et al., 1993; Ciarniello et al.,
 192 2016). The maps have been corrected for roughness, single scattering phase function, and opposition
 193 effects using parameters derived by Ciarnello et al. (2016). The result of the correction procedure is the
 194 reflectance as observed in standard viewing geometry (incidence angle = 30° , emission angle = 0°).
 195 The methods used to produce the VIR data mosaic is fully described in Frigeri et al. (this issue). The
 196 distribution of the 2.7 μm , 3.1 μm and 3.4 μm band depths are shown in Figs. 3, 4, and 5. The
 197 corrected reflectance map at 1.2 μm is shown in Fig. 6, and the spectral slope is shown in Fig. 7.
 198 According to De Sanctis et al. (2015); Ammannito et al. (2016); and De Sanctis et al. (2017), the band
 199 depth at 2.7 μm is correlated with Mg-phyllosilicate abundance, the 3.1 μm band depth is correlated
 200 with NH_4 -phyllosilicate, and the 3.4- μm band depth in Ernutet is correlated with organic material
 201 abundance.

202
 203 A global trend for the band depth at 2.7 μm (Fig. 3) shows a lower amount of phyllosilicates in crater
 204 floors and the crater's ejecta (see also Pasckert et al. (2016)), especially for the three central craters
 205 Ernutet, Liber, and Ikapati and for Gaue crater in the Eastern side of the quadrangle. The highest values
 206 for these endmembers are found in the western, and southwestern sides of the map, where significant
 207 craters are not present.

208
 209 The band depth at 3.1 μm has almost the same behavior of the 2.7- μm band depth (Fig. 4), apart from
 210 two considerations:
 211 - the high latitudes present a systematic deeper band depth than the region at lower latitude;

212 - the Ernutet crater floor and surrounding terrains show an increase in band depth, differently from the
213 2.7- μm band depth and all the other large-sized craters.

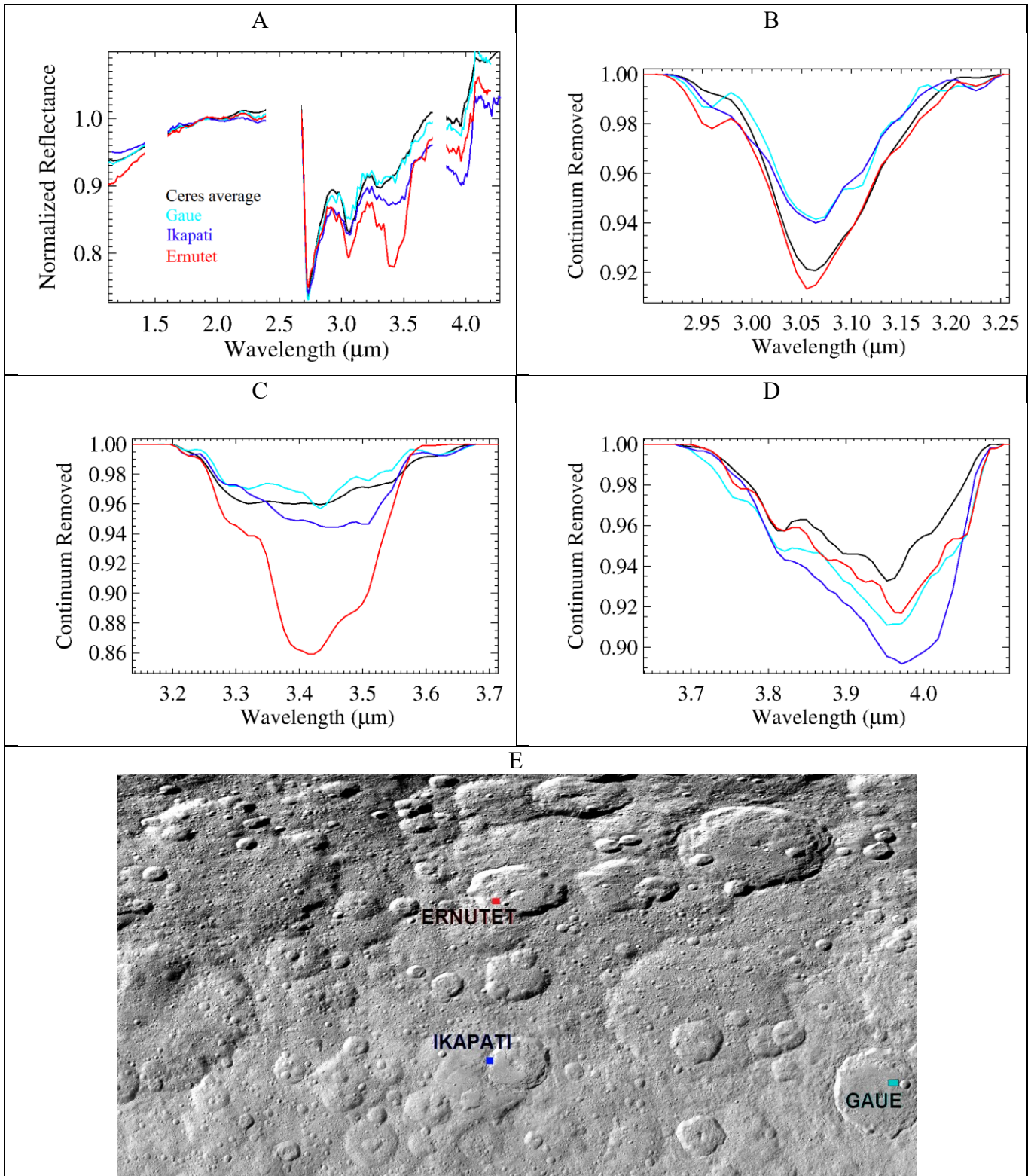
214
215 The deep band depth at 3.4 μm in the Ernutet crater terrain (Fig. 5 and 7C) is an indication of a large
216 abundance of organic aliphatic materials, as discussed in De Sanctis et al. (2017). It is the only case on
217 the whole Ceres' surface where organics features are so evident.

218
219 The photometrically-corrected reflectance level at 1.2 μm returns a good correlation with the band
220 depth at 3.4 μm (see Fig. 6). Moreover, the spectral slope appears redder in the Ernutet crater organic-
221 rich areas (Fig. 7 and 8A). This would point to brighter albedo, and reddish spectra of the organic
222 material than the average surface of Ceres.

223 Conversely, bluer spectra are detected in Ikapati floor and its crater ejecta (see Fig. 7, and 8A) pointing
224 to differences in the composition as discussed in sections 5 and 6.

225
226 We extract average spectra from three regions which appear to be the most peculiar within the
227 quadrangle because of their differences with respect the average Ceres spectrum: Ernutet, Ikapati, and
228 Gaue craters. In particular, carbonates absorptions of Ikapati are broader and shifted toward longer
229 wavelengths with respect the other craters (Fig. 8). This is similar to the bright region in the Occator
230 crater, where this shift has been attributed to a change in the carbonates composition, from Mg-
231 Carbonate to Na-carbonates (De Sanctis et al., 2016). The Ikapati region shows Na-carbonates and
232 could thus have been involved in processes similar to those suggested for the Occator crater, which
233 include a recent aqueous alteration (De Sanctis et al., 2016). We refer to Carrozzo et al. (2017) for a
234 complete discussion on the carbonate distribution on Ceres' surface.

235
236
237
238
239
240
241
242
243
244
245
246
247
248
249
250
251
252
253
254
255
256
257
258
259



260
 261
 262
 263
 264
 265

Figure 8. Panel A: collected spectra normalized at 1.89 μm , from three different crater of Coniraya quadrangle, and the average Ceres spectrum (Ciarniello et al. 2017) for comparison. Panel B-D: spectral range centered on the main absorption bands, after smoothing and continuum removed. Each spectrum is an average of tens of pixel taken from the region indicated in Panel E.

266 5. Spectral Modeling

267

268 To obtain an information on the abundances of the minerals making up the surface, we used a
269 quantitative spectral analysis of the composition using Hapke's radiative transfer model (Hapke 1993,
270 2012) as described by Ciarniello et al. (2011) and Raponi et al. (2016). The whole formulation of the
271 bidirectional reflectance (r) is:

272

$$273 \text{ Eq. 1} \quad r = \frac{SSA}{4\pi} \frac{\mu_0}{\mu + \mu_0} [B_{SH}p(g) + H(SSA, \mu)H(SSA, \mu_0) - 1] \times S(i, e, g, \theta) B_{CB}$$

274

275 Where i , e , g are the incidence, emission, and phase angles, respectively, and μ_0 , μ are the cosines of the
276 incidence and emission angles. These parameters come from the shape model and position of the
277 spacecraft at the time of observation. The parameters that contain most of the spectral information are
278 the single scattering albedo (SSA), and the related Ambartsumian–Chandrasekhar functions $H(SSA, \mu)$
279 describing the multiple scattering components.

280 Other parameters describe the photometric behavior as a function of the viewing geometry, especially
281 the phase function; they are:

- 282 • the single particle phase function $p(g)$,
- 283 • the shadow hiding opposition effect $B_{SH}(g)$,
- 284 • the coherent back-scattering opposition effect $B_{CB}(g)$,
- 285 • the shadow function modelling large-scale roughness $S(i, e, g, \theta)$, with θ being the average
286 surface slope.

287 These photometric parameters are fixed after Ciarniello et al. (2015), who defined the average
288 scattering properties of Ceres' regolith. The spectral properties are mainly affected by the SSA
289 parameters. The latter have been modeled for an intimate mixing between different minerals, which
290 implies that the particles of the end-member materials are in contact with each other and all are
291 involved in the scattering of a single photon. The SSA of each mineral is defined starting from their
292 grain size and their optical constants as described in Hapke (2012). The optical constants are derived
293 from laboratory measurements (Table 1) with the method described by Carli et al. (2014).

294 The average SSA of the regolith is defined through the weights p , which represent the relative
295 abundances of the minerals. The weight p_i is defined as the cross section of the grains of the i th mineral
296 as a fraction of the area. p is also a volume fraction, assuming grain sizes are equal for all minerals.
297 Hereafter we refer to the weights p as “abundances”.

298

$$299 \text{ Eq. 2} \quad SSA = SSA_1p_1 + SSA_2p_2 + SSA_3p_3 + .. \quad \text{with: } p_1 + p_2 + p_3 + .. = 1$$

300

301 The best-fitting result is obtained by comparison of the model with the measured spectra, applying the
302 Levenberg–Marquardt method for non-linear least-squares multiple regression (Marquardt 1963).

303 Free model parameters to be retrieved are:

- 304 (i) abundances of the end-members;
- 305 (ii) grain size of the regolith (assumed equal for all end-members);
- 306 (iii) a multiplicative constant of the absolute level of reflectance of the model in order to account for
307 uncertainties in the radiometric and photometric accuracies, as well as errors on the local geometry
308 information due to unresolved shadows and roughness;
- 309 (iv) a slope added to the model in order to better fit the measured spectrum: in some cases, the
310 measured spectra present an artificial slope where high signal contrast is measured between adjacent
311 pixels, like regions near shadows. This is due to a varying spatial point spread function towards longer
312 wavelengths (Filacchione 2006);

313 (v) temperature and effective emissivity (Davidsson et al., 2009). The latter is the product of the
 314 directional emissivity (Hapke 2012) and a free parameter used to account for unresolved shadow and
 315 the structure of the surface (Davidsson et al. 2009). Its interpretation is outside the scope of this work.

316
 317 The total radiance is modeled by accounting for both the contributions of the reflected sunlight, and the
 318 thermal emission:

319
 320 Eq. 3
$$Rad = r \times \frac{F_{\odot}}{D^2} + \varepsilon_{eff} \times B(\lambda, T)$$

321
 322 where r is the Hapke bidirectional reflectance (Eq.1), F_{\odot} is the solar irradiance at 1 AU, D is the
 323 heliocentric distance (in AU), ε_{eff} is the effective emissivity, $B(\lambda, T)$ is the Planck function. Thus, the
 324 estimation of the thermal emission discussed in Section 3 is done simultaneously with the reflectance
 325 modeling in order to yield a consistent result between these two contributions to the total signal
 326 measured.

327 The SSA is modeled starting from minerals already discussed in De Sanctis et al. (2015, 2016) (see
 328 Table 1) which are related to the average Ceres surface.

329
 330
 331
 332

Mineral	Type	Sample ID
Antigorite	Mg-phyllsilicate	AT-TXH-007
Dolomite	Mg-Ca-carbonate	CB-EAC-003
NH ₄ -montmorillonite	NH ₄ -phyllsilicate	JB-JLB-189
Magnetite	Dark material	MG-EAC-002
Heated Natrite	Na-carbonate	CB-EAC-034-C
Kerite	Organic-aliphatics	MA-ATB-043

333 **Table 1.** End-members used in calculating optical constants of the mineral types. Spectra are taken from the
 334 Relab spectral database.

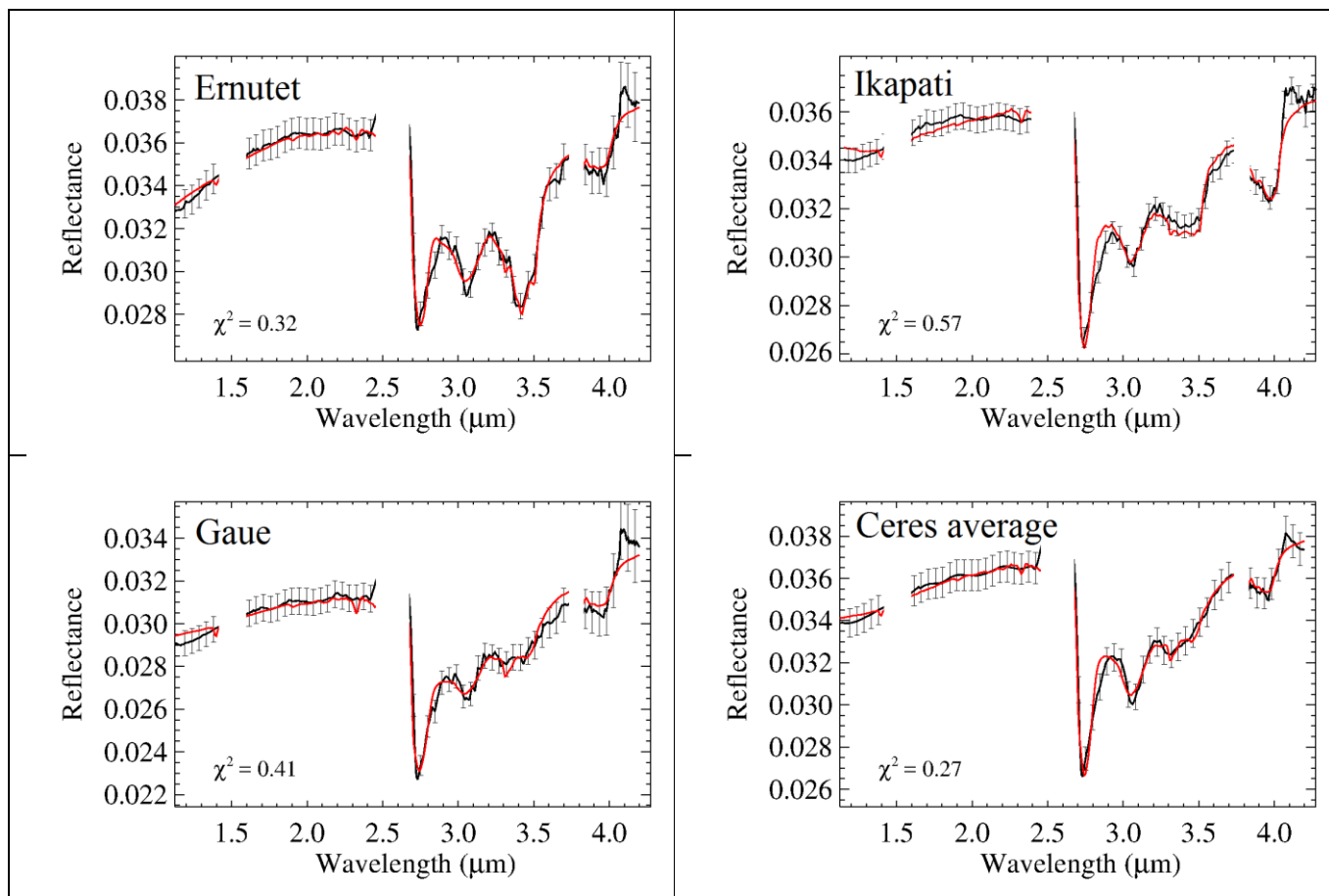
335
 336

337 On Ceres' surface the predominant component is a dark material, whose identification is challenging,
 338 because its spectrum is featureless, except for the tentative absorption band centered at 1 μm , which
 339 can be attributed to iron (Fe). We found a good fit with magnetite (Fe_3O_4), however, a large amount of
 340 Fe is not consistent with GRAND measurements (Prettyman et al. 2017). More likely dark surface of
 341 Ceres should be composed by a large amount of carbon bearing material, being carbonaceous chondrite
 342 its close meteoritic analogue (Chapman, C. R. & Salisbury, J. W., 1973, McSween et al., 2017).
 343 Moreover, we emphasize that the model used in this work is only based on spectral features, being the
 344 absolute signal level of the model adjusted with the multiplicative constant and the additional slope.

345
 346 We apply the model to the average spectra of Ernutet, Ikapati and Gaue shown in Fig. 8, which turned
 347 out to be peculiar from the analysis of the quadrangle (previous section). The best fit are shown in Fig.
 348 9, and the retrieved parameters in table 2.

349 We also apply the spectral modeling to each pixel of the observations covering the whole area of the
 350 three craters. The abundances of the endmembers have been retrieved and projected (Fig. 10-12). The
 351 grain size retrieved was in all cases of the order of 100 μm , without clear variations on the maps. Thus
 352 we decided to fix this value in the fitting procedure.

353
354



355 **Figure 9.** Measured data with error bars of calibration uncertainties (black), and models (red), for the 4 average
356 spectra shown in Fig. 8A. Retrieved parameters are shown in table 2.

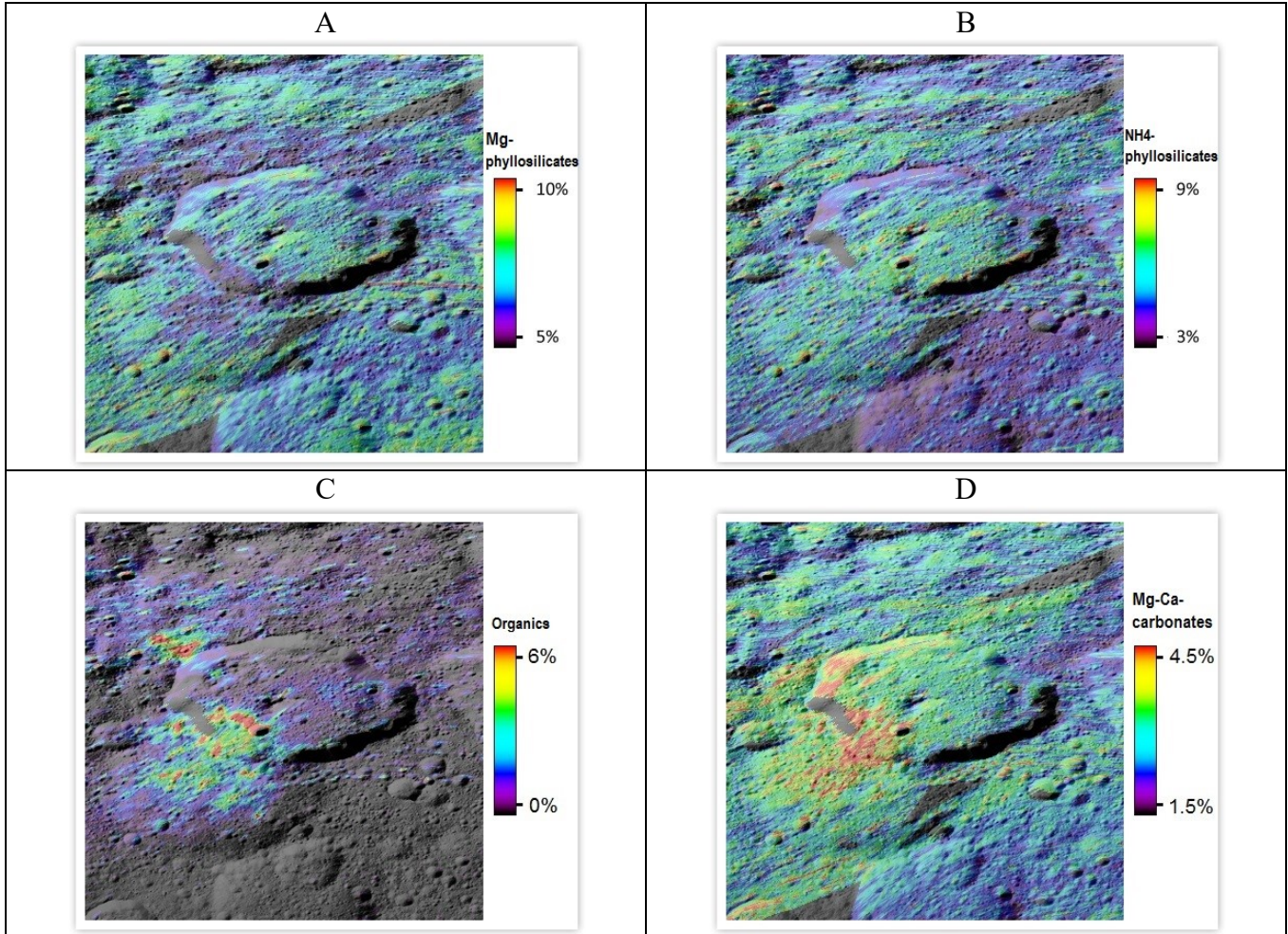
357
358
359

	Ernutet	Ikapati	Gaue	Ceres Average
Mg-phyllsilicates	6.6%	5.8%	6.4%	6.2%
NH ₄ -phyllsilicates	7.5%	3.3%	3.8%	7.0%
Mg-Ca-carbonate	3.6%	2.3%	2.2%	2.2%
Na-carbonate	0.0%	3.3%	0.0%	0.0%
Organics	5.6%	0.0%	0.0%	0.0%

360 **Table 2.** Retrieved abundances from the best fits shown in Fig. 9. In all cases the rest of the composition is a
361 dark neutral material as described in the text.

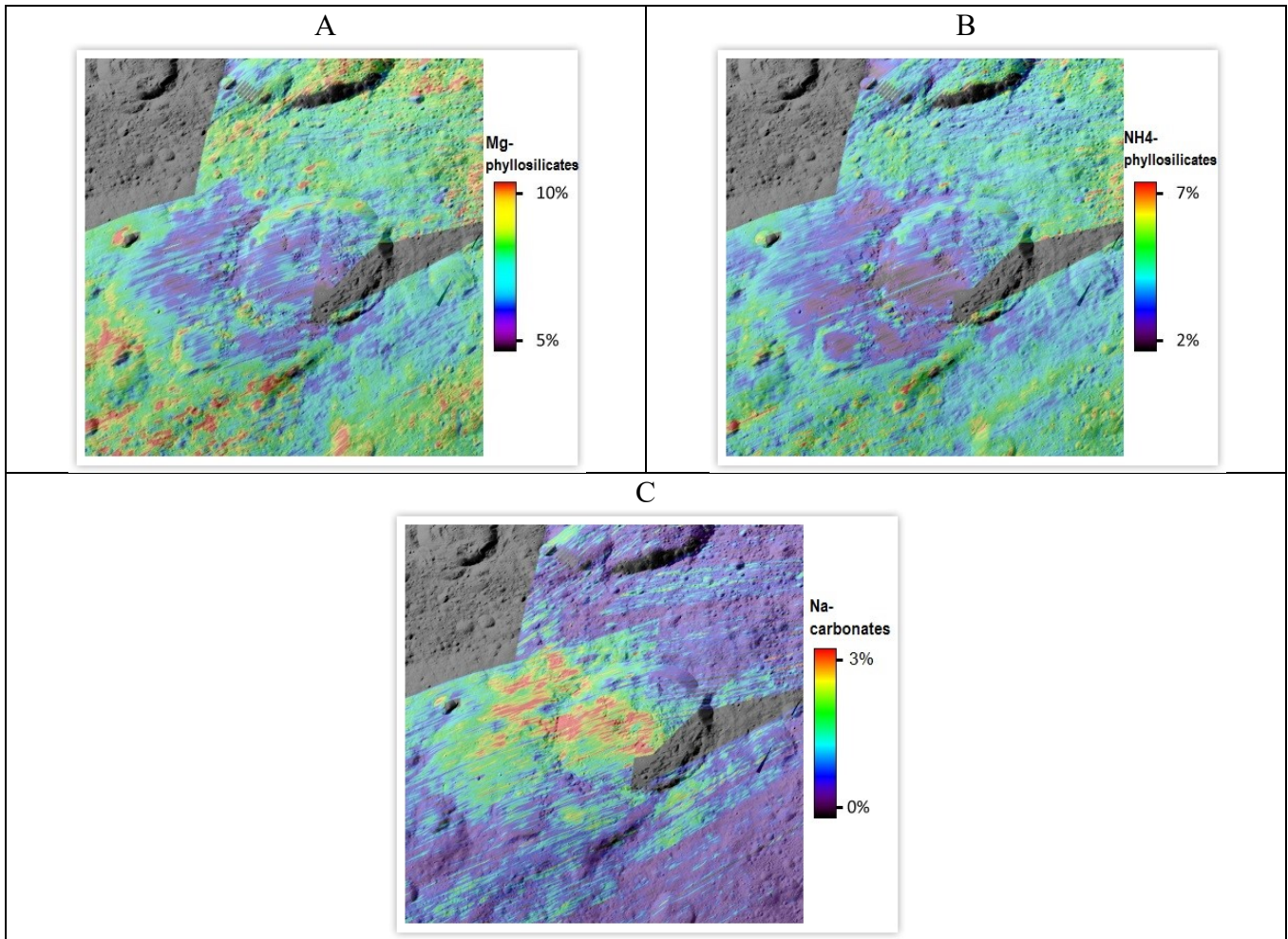
362
363
364
365
366
367
368
369

370
371
372

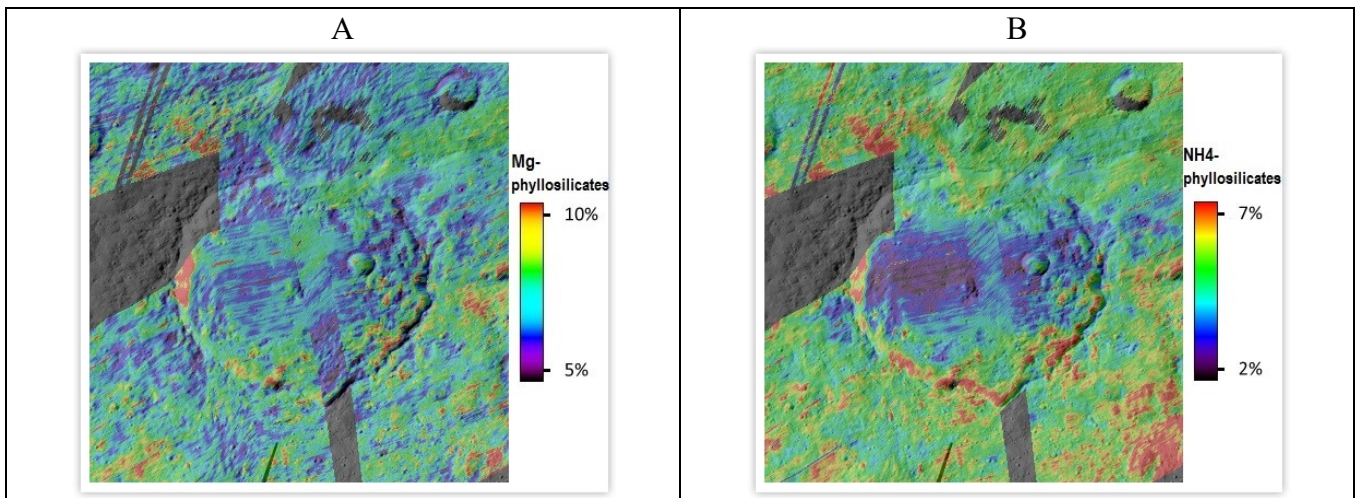


373 **Figure 10.** Distributions of the abundances of the modeled endmembers of the Ernutet crater. Panel A: Mg-
374 phyllosilicates, panel B: NH₄-phyllosilicate, panel C: organics, panel D: Mg-Ca-carbonates.
375

376
377
378
379
380
381
382
383
384
385
386
387
388
389
390



391 **Figure 11.** Distributions of the abundances of the modeled endmembers of the Ikapati crater. Panel A: Mg-
 392 phyllosilicates, panel B: NH₄-phyllosilicate, panel C: Na-carbonates. Other end-members abundances are not
 393 shown because they do not present significant differences with respect the average surface.
 394



395 **Figure 12.** Gaue crater. Mg-phyllsilicates and NH₄-phyllosilicate abundances. Other parameters are not shown
 396 because they do not present significant differences with respect the average surface.
 397
 398

399 *Ernutet*

400 Maps of Fig. 10C shows that abundance distribution of organics in Ernutet crater clearly define two
401 regions with higher concentration:

402 - a larger region in the south-western rim with the higher concentration on the crater floor, but
403 extending outside the crater

404 - a smaller region in the northern-western rim, located outside the crater floor.

405 With the resolution of the map (~400 m/px) we obtain a maximum concentration of 6%. However, we
406 cannot exclude that non-resolved areas can contain more organics. The same consideration is valid for
407 all the other abundances retrieved, and discussed hereafter. The rest of the surface appear to be devoid
408 of organics. However, from the modeling we cannot exclude an amount < 1%.

409 Larger amount of Mg-phyllsilicates (Fig 10A) is mapped inside the floor of Ernutet, up to 8-9%. The
410 surrounding region of the rim are slightly depleted with respect the average Ceres surface. In particular
411 the region with higher concentration of organics present a lower amount of Mg-phyllsilicates (5-6%).

412 Differently from the Mg-phyllsilicates, organic-rich regions contain larger amount of NH₄-
413 phyllsilicates (up to 8-9% as shown in Fig. 10B). Eastern part of the map presents lower amount of
414 NH₄-phyllsilicates (4-5%), while the floor of the crater has an heterogeneous amount.

415 Map of carbonates (Fig. 10D) shows an interesting correlation with the larger/southern organic-rich
416 region. From modeling, carbonates are up to 4.5% in the southern part of the floor. The
417 smaller/northern organic-rich region, does not present such a good correlation with carbonates.

418

419 *Ikapati*

420 Phyllsilicates maps of Ikapati crater shown in figure 11A and 11B, indicate a clear correlation
421 between OH and NH₄ stretching in this crater. Lower amount has been found in the crater floor and in
422 the western ejecta. In the same areas larger concentration of Na-carbonates has been derived from the
423 model (up to 3%). Those carbonates are absent in the average Ceres surface, and only present in small
424 specific areas (Palomba et al., submitted to Icarus), such as the faculae of the Occator crater.

425

426 *Gaue*

427 Differently from Ikapati crater, phyllsilicates maps of Gaue (Figs. 12A and 12B) are not well
428 correlated each other: the map of Mg-phyllsilicates has an heterogeneous distribution with values
429 ranging from 5 to 10%, while the map of NH₄-phyllsilicate clearly presents a lower amount on the
430 crater floor (2-3 %), and about 6% outside it. However, the two end-member are well correlated in a
431 small region in the north/western part of the map, were larger amount of both Mg and NH₄-
432 phyllsilicates have been derived: respectively 10% and 7%.

433

434

435 **6. Discussion and Conclusions**

436 From the analysis of the Coniraya quadrangle, some relevant characteristics emerge. Here we discuss
437 the major findings in the general context of Ceres' surface.

438

439 *Phyllsilicates distribution*

440 The band depth at 2.7 and 3.1 μm mapped in this work are both indicative of phyllsilicate abundance,
441 and relative differences in their distributions are detectable (e.g., between Ikapati and Gaue craters).
442 This was also highlighted by Ammannito et al. (2016) as a general result for Ceres' surface.

443 The floor of the freshest and largest craters present smaller band depth at 2.7 μm and 3.1 μm .

444 The modeling performed for Ernutet, Ikapati, and Gaue craters reveals that the smaller band depth can
445 be interpreted as a lower amount of Mg/NH₄-phyllsilicates. Smaller phyllsilicates band associates
446 with relatively young crater seems quite common on Ceres' surface (De Sanctis et al., this issue),

447 which may be the result of a volatile depletion due to impact heating. A noticeable exception is
448 represented by the large-scale depression of Vendimia Planitia, located in the eastern adjacent
449 quadrangles. The measured phyllosilicate absorptions at 2.7 and 3.1 μm , in two main craters located in
450 this area, Dantu (Stephan et al., this issue) and Kerwan (Palomba et al., this issue), are stronger than its
451 surrounding areas, and they actually are the deepest phyllosilicate absorptions measured on Ceres
452 (Stephan et al., this issue). This observed trend may reveal a change in the composition of Ceres' crust
453 with increasing depth below the topographic mean (Stephan et al., this issue).

454

455 The Mg and NH_4 -phyllosilicates modeled present different depletion in the three craters mapped in Fig.
456 10-12. The cases that stand out are the high contrast for Ikapati crater floor and ejecta (Fig. 11A, 11B),
457 and the NH_4 -phyllosilicates on the Gaue crater floor (Fig. 12B).

458 This would point to a complex picture in which different processes can concur to determine the
459 volatiles abundances during the impact (e.g. energy released by the impactor, depth of excavation),
460 after the impact (e.g. aqueous alteration, hydrothermal activity, lateral mixing by micrometeoritic
461 impacts, space weather), and could also reflect heterogeneities on Ceres' surface preexistent to the
462 impact event.

463

464

465 *Ikapati crater and ejecta*

466 As discussed in the previous section, Ikapati fresh crater shows slightly smaller band depth at 2.7 μm
467 and 3.1 μm , which would mean a lower concentration of Mg/ NH_4 -phyllosilicates. By taking into
468 account the average spectrum shown in Fig. 10, we notice other relevant differences: larger absorption
469 band of carbonates, and bluer spectral slope. Moreover, the band center of the carbonates absorption
470 band shows a shift from 3.95 to 4.0 μm (see Fig. 8D), similar to the bright region in the Occator crater,
471 where this shift has been attributed to a change in the carbonates composition, from Mg-Carbonate to
472 Na-Carbonates (De Sanctis et al., 2016; Longobardo et al., this issue). The Ikapati region could thus
473 have been involved in similar processes, as suggested for the Occator crater, which include a recent
474 aqueous alteration (De Sanctis et al., 2016). However, in Ikapati the Na-carbonate is spread in the floor
475 and ejecta, rather than being concentrated in specific regions inside the crater floor. This can be the
476 result of the impact event of Ikapati that spread bright material previously concentrated in faculae like
477 in Occator crater. This hypothesis would point to a unique formation process for all bright material
478 present on the surface as suggested by (Stein et al., submitted), being their differences due to the
479 following story of impact events.

480 Contrarily to the slow process occurring to form the bright material, the volatile depletion due to the
481 impact induced heating could be fast, and it can explain the correlation of the lower amount of hydrated
482 (OH- stretching) and ammoniated phyllosilicates (NH_4 -stretching) in correspondence of the ejecta.

483

484 *Ernutet crater and organic-rich regions*

485 The Ernutet crater is a unique feature of Ceres' surface, revealing a large amount of organic material
486 that is mapped in this work by the 3.4- μm absorption band, and the abundance map of Fig. 10C. This
487 absorptions is characteristic of the symmetric and antisymmetric stretching frequencies of methyl
488 (CH_3) and methylene (CH_2) functional groups, typical of aliphatic hydrocarbons (F.-R. Orthous-
489 Daunay et al., 2013). The model performed in the present work (Fig 9A) and in (De Sanctis et al. 2016)
490 shows that Ceres organics signatures are very similar with the organic bands of terrestrial hydrocarbons
491 such as kerite.

492 An evident correlation with organics distribution has been found with the absolute level of reflectance
493 at 1.2 μm (Fig. 6), and the reddish slope (Fig. 7), revealing a possible constraint on the optical
494 properties of the organic material: brighter and more reddish than the average surface of Ceres.

495 The abundance map of organics shown in Fig. 10C clearly define two regions with higher
496 concentration of organics. In the work of De Sanctis et al. (2016) these two regions were labeled as
497 region A (southern) and B (northern). In the same two regions we derived:

- 498 1) smaller abundance of Mg-phyllsilicates (Fig. 10A);
- 499 2) slightly larger abundance of NH₄-phyllsilicates (Fig. 10B);
- 500 3) only in the southern region larger abundance of Mg-Ca-carbonates (Fig. 10D);

501 De Sanctis et al. 2016 suggested an endogenous origin of the organics, on the base of the larger
502 presence of carbonates, (and slight larger presence of NH₄-phyllsilicates), both being products of an
503 hydrothermal activity together with the organics. An exogenous origin would require further
504 explanations about the correlation with minerals (carbonates, NH₄-phyllsilicates) extensively present
505 on Ceres surface, but unseen in the asteroid belt with the same amount.

506 The uniqueness of such organic-rich region would point to an uncommon condition over Ceres'
507 surface. However, the asymmetry of the retrieved parameters in the two regions (point 3), would point
508 to formation processes under different thermophysical and/or chemical conditions, occurring very close
509 each other, but both favorable for the organics formation.

510
511 Further efforts are needed to assess the mechanism responsible for the formation and transport to the
512 surface of minerals which should have a different origin with respect the common Ceres minerals, like
513 organics and Na-carbonates.

514 The uniqueness of specific places on Ceres surface, together with the diversity of mineralogy is an
515 indication of a complex environment typical of an active body.

516

517

518

519

520 **Acknowledgments**

521 VIR is funded by the Italian Space Agency-ASI and was developed under the leadership of INAF-
522 Istituto di Astrofisica e Planetologia Spaziali, Rome-Italy. The instrument was built by Selex-Galileo,
523 Florence-Italy. The authors acknowledge the support of the Dawn Science, Instrument, and Operations
524 Teams. This work was supported by ASI and NASA.

525

526

527

528 **References**

529 Ammannito, E., De Sanctis, M.C., Ciarniello, M., Frigeri, A., Carrozzo, F.G., Combe, J.-Ph., Ehlmann,
530 B.L., Marchi, S., McSween, H.Y., Raponi, A., Toplis, M.J., Tosi, F., Castillo-Rogez, J.C., Capaccioni,
531 F., Capria, M.T., Fonte, S., Giardino, M., Jaumann, R., Longobardo, A., Joy, S.P., Magni, G., McCord,
532 T.B., McFadden, L.A., Palomba, E., Pieters, C.M., Polanskey, C.A., Rayman, M.D., Raymond, C.A.,
533 Schenk, P.M., Zambon, F., Russell, C.T., 2016. Distribution of phyllosilicates on the surface of Ceres.
534 *Science* 353 (6303), id.aaf4279. Doi: 10.1126/science.aaf4279.

535

536 Carrozzo, F.G., Raponi, A., De Sanctis, M.C., Ammannito, E., Giardino, M., D'Aversa, E., Fonte, S.,
537 Tosi, F., 2016. Artifacts reduction in VIR/Dawn data. *Rev. Sci. Instrum.* 87 (12), id.124501. Doi:
538 10.1063/1.4972256.

539

540 Carrozzo, F.G., De Sanctis, M.C., Raponi, A., Ammannito, E., Castillo-Rogez, J.C., Ehlmann, B.L.,
541 Marchi, S., Stein, N., Ciarniello, M., Tosi, F., Capaccioni, F., Capria, M.T., Fonte, S., Formisano, M.,
542 Frigeri, A., Giardino, M., Longobardo, A., Magni, G., Palomba, E., Zambon, F., Raymond, C.A.,
543 Russell, C.T., 2017a. Nature, formation and distribution of Carbonates on Ceres. Submitted to Science.
544 Under review.

545

546 Chapman, C. R. & Salisbury, J. W. Comparisons of meteorite and asteroid spectral reflectivities. *Icarus*
547 19, 507–522 (1973).

548

549 Ciarniello, M., De Sanctis, M.C., Ammannito, E., Raponi, A., Longobardo, A., Palomba, E., Carrozzo,
550 F.G., Tosi, F., Li, J.-Y., Schröder, S.E., Zambon, F., Frigeri, A., Fonte, S., Giardino, M., Pieters, C.M.,
551 Raymond, C.A., Russell, C.T., 2017. Spectrophotometric properties of dwarf planet Ceres from the
552 VIR spectrometer on board the Dawn mission. *Astron. Astrophys.* 598, id.A130. Doi: 10.1051/0004-
553 6361/201629490.

554

555 Combe, J.-Ph., McCord, T.B., Tosi, F., Ammannito, E., Carrozzo, F.G., De Sanctis, M.C., Raponi, A.,
556 Byrne, S., Landis, M.E., Hughson, K.H.G., Raymond, C.A., Russell, C.T., 2016. Detection of local H₂O
557 exposed at the surface of Ceres. *Science* 353 (6303), id.aaf3010. Doi: 10.1126/science.aaf3010.

558

559 Combe, J.-Ph., Raponi, A., Tosi, F., De Sanctis, M.C., Carrozzo, F.G., Zambon, F., Ammannito, E.,
560 Hughson, K.H.G., Nathues, A., Hoffmann, M., Platz, T., Thangjam, G., Schorghofer, N., Schröder,
561 S.E., Byrne, S., Landis, M.E., Ruesch, O., McCord, T.B., Johnson, K.E., Singh, S.M., Raymond, C.A.,
562 Russell, C.T., 2017a. Exposed H₂O-rich areas detected on Ceres with the Dawn Visible and InfraRed
563 mapping spectrometer. Submitted to *Icarus* (this issue). Under review.

564

565 De Sanctis, M.C., Coradini, A., Ammannito, E., Filacchione, G., Capria, M.T., Fonte, S., Magni, G.,
566 Barbis, A., Bini, A., Dami, M., Fikai-Veltroni, I., Preti, G., and the VIR Team, 2011. The VIR
567 Spectrometer. *Space Sci Rev.* 163, Issue 1–4, 329-369. Doi: 10.1007/s11214-010-9668-5.

568

569 De Sanctis, M.C., Ammannito, E., Raponi, A., Marchi, S., McCord, T.B., McSween, H.Y., Capaccioni,
570 F., Capria, M.T., Carrozzo, F.G., Ciarniello, M., Longobardo, A., Tosi, F., Fonte, S., Formisano, M.,
571 Frigeri, A., Giardino, M., Magni, G., Palomba, E., Turrini, D., Zambon, F., Combe, J.-Ph., Feldman,
572 W., Jaumann, R., McFadden, L.A., Pieters, C.M., Prettyman, T., Toplis, M., Raymond, C.A., Russell,
573 C.T., 2015. Ammoniated phyllosilicates with a likely outer Solar System origin on (1) Ceres. *Nature*
574 528 (7581), 241-244. Doi: 10.1038/nature16172.

575

576 De Sanctis, M.C., Raponi, A., Ammannito, E., Ciarniello, M., Toplis, M.J., McSween, H.Y., Castillo-
577 Rogez, J.C., Ehlmann, B.L., Carrozzo, F.G., Marchi, S., Tosi, F., Zambon, F., Capaccioni, F., Capria,
578 M.T., Fonte, S., Formisano, M., Frigeri, A., Giardino, M., Longobardo, A., Magni, G., Palomba, E.,

579 McFadden, L.A., Pieters, C.M., Jaumann, R., Schenk, P., Mugnuolo, R., Raymond, C.A., Russell, C.T.,
580 2016. Bright carbonate deposits as evidence of aqueous alteration on (1) Ceres. *Nature* 536 (7614), 54-
581 57. Doi: 10.1038/nature18290.

582

583 De Sanctis, M.C., Ammannito, E., McSween, H.Y., Raponi, A., Marchi, S., Capaccioni, F., Capria,
584 M.T., Carrozzo, F.G., Ciarniello, M., Fonte, S., Formisano, M., Frigeri, A., Giardino, M., Longobardo,
585 A., Magni, G., McFadden, L.A., Palomba, E., Pieters, C.M., Tosi, F., Zambon, F., Raymond, C.A.,
586 Russell, C.T., 2017a. Localized aliphatic organic material on the surface of Ceres. *Science* 355 (6326),
587 719-722. Doi: 10.1126/science.aaj2305.

588

589 Frigeri, A. De Sanctis, M.C., Ammannito, E., Tosi, F., Ciarniello, M., Zambon, F., Carrozzo, F.G.,
590 Raponi, A., McCord, T.B., Raymond, C.A., Russell, C.T., 2017. The spectral parameter maps of Ceres
591 from NASA/DAWN VIR data. Submitted to *Icarus* (this issue). Under review.

592

593 Hapke B., *Theory of reflectance and emittance spectroscopy*, 1993.

594

595 Hapke B., 1993, *Theory of reflectance and emittance spectroscopy* Second Edition, 2012

596

597 Konopliv, A. S.; Asmar, S. W.; Bills, B. G.; Mastrodemos, N.; Park, R. S.; Raymond, C. A.;
598 Smith, D. E.; Zuber, M. T. *The Dawn Gravity Investigation at Vesta and Ceres. Space Science*
599 *Reviews*, 163, pp. 461-486

600

601 Longobardo, A., et al., 2017. Mineralogy of the Occator quadrangle. Submitted to *Icarus* (this issue).
602 Under review.

603

604 McSween, H. Y.; Castillo-Rogez, J.; Emery, J. P.; De Sanctis, M. C.; Dawn Science Team.
605 *Rationalizing the Composition and Alteration of Ceres. LPI Contribution No. 1903*, p.1258, 2016.

606

607 Orthous-Daunay, F.-R.; Quirico, E.; Beck, P.; Brissaud, O.; Dartois, E.; Pino, T.; Schmitt, B., Mid-
608 infrared study of the molecular structure variability of insoluble organic matter from primitive
609 chondrites. *Icarus* 223, 534–543, 2013.

610

611 Palomba, E., Longobardo, A., De Sanctis, M.C., Carrozzo, F.G., Galiano, A., Zambon, F., Raponi, A.,
612 Ciarniello, M., Stephan, K., Williams, D., Ammannito, E., Capria, M.T., Fonte, S., Giardino, M., Tosi,
613 F., Raymond, C.A., Russell, C.T., 2017. Mineralogical mapping of the Kerwan quadrangle on Ceres.
614 Submitted to *Icarus* (this issue). Under review.

615

616 Pasckert, J. H.; Hiesinger, H.; Williams, D. A.; Crown, D. A.; Mest, S. C.; Buczkowski, D. L.; Scully,
617 J. E. C.; Schmedemann, N.; Jaumann, R.; Roatsch, T.; Preusker, F.; Nass, A.; Nathues, A.; Hoffmann,
618 M.; Schäfer, M.; De Sanctis, M. C.; Raymond, C. A.; Russell, C. T. Geologic Mapping of the Ac-H-2
619 Coniraya Quadrangle of Ceres from NASA's Dawn Mission. 47th Lunar and Planetary Science
620 Conference, LPI Contribution No. 1903, p.1450, 2016.

621

622 N. Stein, B. L. Ehlmann, E. Palomba, M. C. De Sanctis, A. Nathues, H. Hiesinger, E. Ammannito, C.
623 A. Raymond, R. Jaumann, A. Longobardo, C. T. Russell, The Formation and Evolution of Bright Spots
624 on Ceres, submitted to *Icarus*.

625

626 Prettyman, Thomas H.; Feldman, William C.; McSween, Harry Y.; Dingler, Robert D.;
627 Enemark, Donald C.; Patrick, Douglas E.; Storms, Steven A.; Hendricks, John S.;
628 Morgenthaler, Jeffery P.; Pitman, Karly M.; Reedy, Robert C. Dawn's Gamma Ray and Neutron
629 Detector. *Space Science Reviews*, 163, pp. 371-459

630

631 Raponi, A.; Ciarniello, M.; Capaccioni, F.; Filacchione, G.; Tosi, F.; De Sanctis, M. C.; Capria, M. T.;
632 Barucci, M. A.; Longobardo, A.; Palomba, E.; Kappel, D.; Arnold, G.; Mottola, S.; Rousseau, B.;
633 Rinaldi, G.; Erard, S.; Bockelee-Morvan, D.; Leyrat, C. The temporal evolution of exposed water ice-
634 rich areas on the surface of 67P/Churyumov–Gerasimenko: spectral analysis. *MNRAS* 462, 2016.

635

636 Roatsch, T., Kersten, E., Matz, K.-D., Preusker, F., Scholten, F., Jaumann, R., Raymond, C.A., Russell,
637 C.T., 2016a. Ceres survey atlas derived from Dawn Framing Camera images. *Planet. Space Sci.* 121,
638 115-120. Doi: 10.1016/j.pss.2015.12.005.

639

640 Roatsch, T., Kersten, E., Matz, K.-D., Preusker, F., Scholten, F., Jaumann, R., Raymond, C.A., Russell,
641 C.T., 2016b. High-resolution Ceres High Altitude Mapping Orbit atlas derived from Dawn Framing
642 Camera images. *Planet. Space Sci.* 129, 103-107. Doi: 10.1016/j.pss.2016.05.011.

643

644 Russell, C. T.; Raymond, C. A. The Dawn Mission to Vesta and Ceres. *Space Science Reviews*, 163,
645 pp. 3-23, 2011.

646

647 Sierks, H., Keller, H.U., Jaumann, R., Michalik, H., Behnke, T., Bubenhausen, F., Büttner, I., Carsenty,
648 U., Christensen, U. Enge, R., Fiethe, B., Gutiérrez-Marqués, P., Hartwig, H., Krüger, H., Kühne, W.,
649 Maue, T., Mottola, S., Nathues, A., Reiche, K.-U., Richards, M.L., Roatsch, T., Schröder, S.E.,
650 Szemerey, I., Tschentscher, M., 2011. The Dawn Framing Camera. *Space Sci Rev.* 163, Issue 1–4, 263-
651 327. Doi: 10.1007/s11214-011-9745-4.

652

653 Singh, S., Combe, J.-Ph., McFadden, L.A., McCord, T.B., Johnson, K.E., Hughson, K.H.G., Zambon,

654 F., Ciarniello, M., Carrozzo, F.G., Ammannito, E., De Sanctis, M.C., Ruesch, O., Stephan, K., Tosi, F.,
655 Longobardo, A., Raymond, C.A., Russell, C.T., 2017. Mineralogy mapping of the Ac-H-5 Fejokoo
656 quadrangle of Ceres. Submitted to *Icarus* (this issue). Under review.

657

658 Stephan, K., Jaumann, R., Zambon, F., Carrozzo, F.G., De Sanctis, M.C., Tosi, F., Ammannito, E.,
659 Longobardo, A., Palomba, E., McFadden, L.A., Krohn, K., Williams, D.A., Raponi, A., Ciarniello, M.,
660 Combe, J.-Ph., Frigeri, A., Roatsch, T., Matz, K.-D., Preusker, F., Raymond, C.A., Russell, C.T.,
661 2017b. Spectral investigation of quadrangle Ac-H-3 of the dwarf planet Ceres – The region of impact
662 crater Dantu. Submitted to *Icarus* (this issue). Under review.

663

664 Tosi, F., Carrozzo F.G., Zambon F., Ciarniello M., Frigeri A., Combe J.-Ph., De Sanctis M.C.,
665 Hoffmann M., Longobardo A., Nathues A., Raponi A., Ammannito E., Krohn K., McFadden L.A.,
666 Palomba E., Pieters C.M., Stephan K., Raymond C.A., Russell C.T., and the *Dawn* Science Team.
667 Mineralogical analysis of the Haulani quadrangle of the dwarf planet Ceres. Submitted to *Icarus* (this
668 issue). Under review.